PAPER

Check for updates

Abundant active-site engineering enables porous Co−N−C electrocatalysts towards superior oxygen reduction reaction activity†

Yue Zhang,[a] Zexuan Du,[a] Huaping Mei,[a] Bingye Song, (ID) *[a] Qianzhi Gou, (ID) *[a] Xiaolin Hu,*[b] Di Qi,[a] Ran Gao[a] and Xianda Sun[c]

The insufficiency of effective active sites and poor stability are identified as primary factors responsible for the performance limitations of non-precious metal carbon-based catalysts towards the oxygen reduction reaction (ORR). Increasing the number of non-precious metal and N−C active sites while achieving their uniform distribution continues to be a major challenge in the advancement of oxygen reduction catalysts. In this work, riboflavin was employed to modify the precursors ZIF-8 and ZIF-67, leveraging the high electronegativity of nitrogen atoms in the isoalloxazine ring to enhance the anchoring effect on metal ions, thereby reducing the agglomeration of Co ions during pyrolysis. Furthermore, during the high-temperature pyrolysis process, the cleavage and integration of nitrogen-containing functional groups in riboflavin not only led to an increase in the doping density of N heteroatoms within the carbon framework but also enriched the pore structure of the catalyst. Co−N active sites and plentiful N−C active sites can be uniformly dispersed within the micro−mesoporous Co−N−C framework, thereby boosting electron transfer rates and enlarging the electrochemically active surface area. The transmission resistance of components can be effectively reduced in the carbon framework with a hierarchical pore structure, which could enhance the rate of oxygen electrocatalytic reduction. Consequently, the obtained Co−N−C catalyst exhibits outstanding catalytic activity in the oxygen reduction reaction comparable to that of commercial Pt/C, along with superior stability and alcohol tolerance.

1 Introduction

Electrochemical conversion devices, such as fuel cells and zinc–air batteries, have attracted significant attention in recent years due to their high energy conversion efficiency and environmental friendliness.[1–4] However, the sluggish kinetics of the cathodic oxygen reduction reaction (ORR) presents a major challenge that limits the practical application of these devices. Consequently, the use of platinum-based catalysts becomes essential to enhance the rate-limiting step. Nevertheless, the scarcity and high cost of platinum resources

pose a substantial barrier to their large-scale deployment.[5] Therefore, there is an urgent need to develop non-platinum catalysts, with carbon-based non-precious metal catalysts emerging as promising alternatives due to their affordability and exceptional ORR activity.[6]

Under adjustable pore structures, various carbon materials, including carbon nanotubes, graphene, and metal–organic frameworks (MOFs), have been utilized as skeletons for the precursors of carbon-based electrocatalysts.[7–9] The synthesis of carbon nanotubes and graphene is inherently complex, presenting significant challenges related to structural regulation and high production costs. In contrast, MOFs, particularly zeolitic imidazolate frameworks (ZIFs), serve as superior precursors for the preparation of carbon-based electrocatalysts.[10] The zinc ions present in ZIF-8 are prone to volatilization, leading to an insufficient number of metal–nitrogen–carbon active sites. Conversely, cobalt ions in ZIF-67 tend to aggregate, resulting in the formation of metal clusters that exhibit reduced activity, which contributes to an uneven distribution of metal active sites.[11,12] To mitigate the limitations associated with individual ZIF structures, a room-temperature co-precipitation method was employed to synthesize composite precursors uti-

[a] International Joint Laboratory on Low Carbon Built Environment of MOE, School of Building Services Science and Engineering, Xi'an University of Architecture and Technology, Xi'an 710055, China. E-mail: bysong@xauat.edu.cn, gqz813@xauat.edu.cn
[b] School of Science, Chongqing Key Laboratory of New Energy Storage Materials and Devices, Chongqing University of Technology, Chongqing 400054, China. E-mail: huxl@cqut.edu.cn
[c] Institute for Advanced Science and Technology, Shandong University, Jinan 250061, China
† Electronic supplementary information (ESI) available. See DOI: https://doi.org/10.1039/d4nr05131a

lizing both ZIF-67 and ZIF-8.[13] During the high-temperature pyrolysis process, the volatilization of zinc ions facilitates the formation of pores and defects, which enhances the dispersion of cobalt ions and enables the construction of efficient and uniformly distributed active sites.[14,15]

The oxygen reduction reaction catalysts synthesized through the direct pyrolysis of ZIF-8 and ZIF-67 precursors in combination demonstrated suboptimal catalytic performance, primarily due to the inadequate formation of effective active sites during the pyrolysis process. To mitigate this issue, various strategies, including heteroatom doping, are commonly employed, which involves the incorporation of elements such as nitrogen,[16] sulfur,[17] phosphorus,[18,19] and boron.[20] Among these, nitrogen doping is particularly favored due to the differences in electronegativity between nitrogen and carbon.[21] The introduction of nitrogen atoms modifies the charge distribution within carbon materials, thereby enhancing the electron transfer rate and improving the reduction efficiency of oxygen molecules. Additionally, the incorporation of nitrogen atoms can induce structural defects in carbon and generate nitrogen-containing functional groups, such as pyrrolic nitrogen, pyridinic nitrogen, and graphitic nitrogen.[22] This process ultimately increases the number of effective active sites.

During the preparation of nitrogen-doped carbon-based catalysts, the nitrogen source plays a vital role as it is a fundamental component of the active sites of the catalyst. The most commonly utilized nitrogen sources are ammonia and melamine. However, the use of ammonia poses challenges in reaction control and raises safety concerns due to its toxicity and volatility.[23] Additionally, melamine is associated with the issue of residual decomposition products.[24] Therefore, it is essential to identify an economical, efficient, and safe alternative nitrogen source. Among various candidates, riboflavin (vb_2) stands out due to its optimal nitrogen-to-carbon ratio, high nitrogen and oxygen content, cost-effectiveness, and low toxicity, making it an ideal candidate as a nitrogen source.[25,26] Furthermore, the controllability of its reaction process and the relatively simple reaction conditions make this a promising candidate as an alternative nitrogen source.

In this work, riboflavin was employed to modify the surface of ZIFs to fabricate a novel oxygen reduction reaction electrocatalyst with a rich porous structure and uniformly distributed active sites. Nitrogen atoms in riboflavin were used to form coordination bonds with metal ions in ZIFs during the co-precipitation process.[27,28] The riboflavin coated on the precursor can be dissociated to the isoalloxazine rings and carbon–nitrogen bonds in the subsequent high-temperature pyrolysis process.[29,30] This process facilitated the incorporation of nitrogen-containing functional groups into the carbon framework, resulting in an increased number of active sites on the catalyst surface and an alteration in the charge distribution of the carbon material. Concurrently, the volatilization of dissociated components at elevated temperatures resulted in an enriched porous structure. The influence of the pyrolysis temperature on the physical and chemical structure, as well as the electro-

chemical performance of the final product, was explored. The stability and the oxygen reduction reaction mechanism of the ORR catalyst were also analyzed.

2 Experimental section

2.1 Synthesis of precursors

The precursors were synthesized *via* co-precipitation reaction at ambient temperature. The specific procedure was as follows: a solution of 0.582 g (2 mmol) of $Co(NO_3)_2 \cdot 6H_2O$ in 20 mL of methanol was prepared to give a pink transparent solution designated A. Similarly, a solution of 0.892 g (3 mmol) of $Zn(NO_3)_2 \cdot 6H_2O$ in 30 mL of methanol was prepared to give a colorless transparent solution designated B. A solution of 1.642 g (20 mmol) of 2-methylimidazole in 24 mL of methanol was prepared, resulting in solution C. Solution D was prepared by dissolving 0.1 g of vb_2 in 20 mL of methanol. Solutions A, B, C, and D were then mixed and co-precipitated at room temperature for 24 hours, followed by an additional 24 hours of standing. The reaction-derived precipitate was subjected to multiple washings *via* centrifugation (10 000 rpm for 10 minutes) and subsequently vacuum-dried under an ethanol atmosphere at 70 °C for 24 hours. This process yielded the riboflavin-doped ZIF-8&ZIF-67 precursors, designated as ZIF-8&ZIF-67-vb_2. For the control experiment, riboflavin was excluded, and following the same procedural steps, ZIF-8&ZIF-67 precursors were obtained (designated as ZIF-8&ZIF-67).

2.2 Synthesis of the Co_v–N–C sample

The ZIF-8&ZIF-67-vb_2 precursors were placed in a tube furnace and heated from room temperature to 850 °C at a rate of 3 °C per minute. Following a three-hour period at the specified temperature, the furnace was permitted to cool naturally to room temperature, resulting in a black powder designated Co_v–N–C_{850}. To ascertain the impact of pyrolysis temperature on the electrochemical characteristics of the product, the pyrolysis temperature was altered, and the experiments were conducted anew. The resulting catalysts were defined as Co_v–N–C_x, where x corresponds to the pyrolysis process at temperatures of 750 °C, 850 °C, 950 °C, 1050 °C and 1150 °C. In order to ascertain the effect of riboflavin on the electrochemical performance of the final samples, the ZIF-8&ZIF-67 precursors were placed in a tubular furnace and heated at a consistent rate to the same target temperature. The catalysts obtained from this process were designated as Co–N–C_{850}.

3 Results and discussion

3.1 Morphological characterizations

The synthesis mechanism of the Co_v–N–C_{850} catalyst is illustrated in Fig. 1. During ZIF-8 and ZIF-67 synthesis, riboflavin is incorporated, where its isoalloxazine ring acts as a redox-active moiety that coordinates with ZIF metal ions *via* a revers-
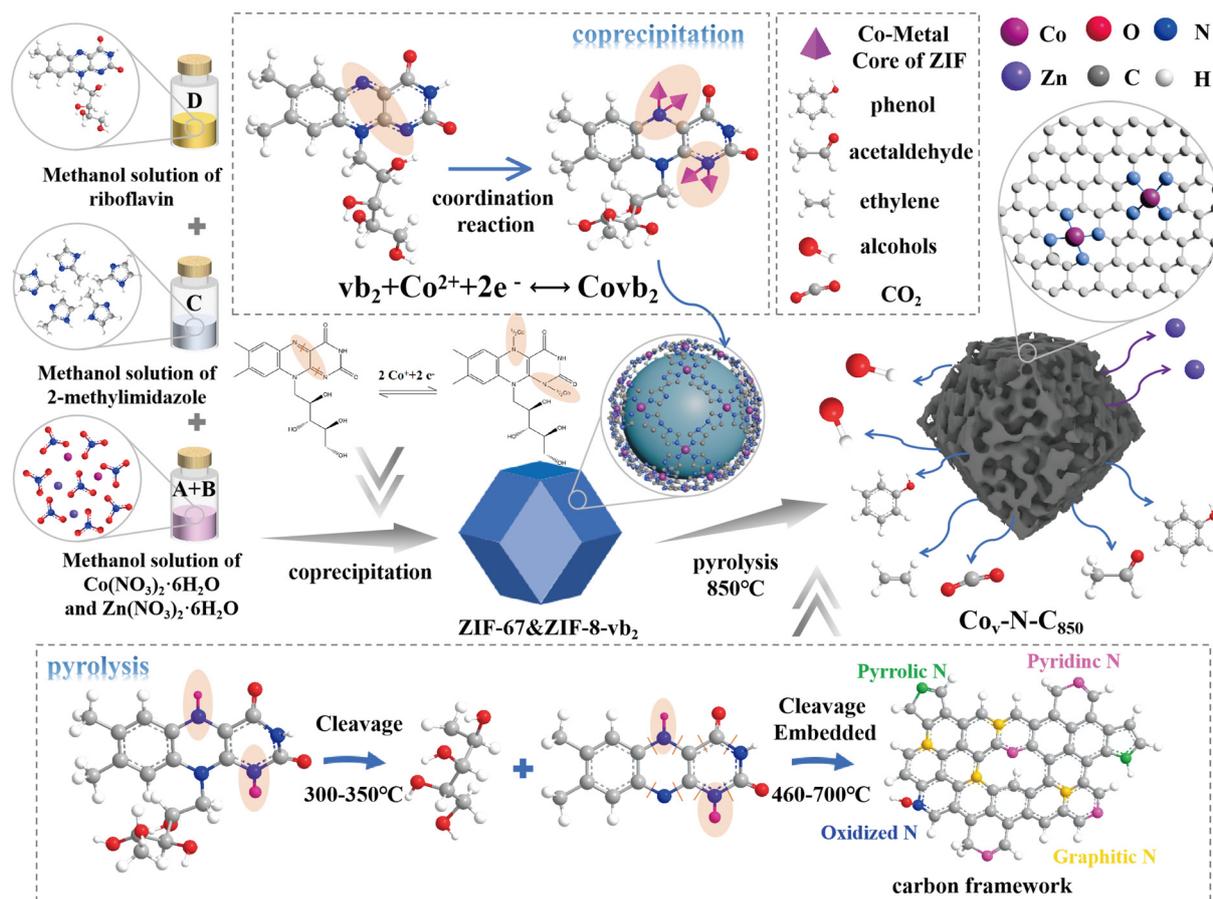
Fig. 1 Schematic illustration of the synthesis route of the Co−N−C catalyst.

ible two-electron transfer mechanism. Subsequent high-temperature pyrolysis induces thermal degradation of riboflavin, cleaving the isoalloxazine ring and C−N bonds. This process generates volatile compounds such as alcohols, ethylene, acetaldehyde, phenol, and CO_2, which create abundant mesopores within the carbon framework. Concurrently, carbon and nitrogen heteroatoms integrate into the carbon matrix, forming nitrogen-containing functional groups that increase active site density, ultimately yielding the Co_v–N–C_{850} catalyst.

As shown in Fig. 2(a–c), the riboflavin-doped Co_v–N–C_{850} catalyst retains the dodecahedral morphology observed in the undoped Co–N–C_{850} catalyst. Variations in pyrolysis temperature do not significantly alter this structural configuration (Fig. S1†). The average particle size of Co_v–N–C_{850} (160 nm) is smaller than that of Co–N–C_{850} (180 nm). This size disparity can be attributed to two factors. First, ZIF-8 exerts a suppressive effect on the crystal growth of ZIF-67.[31] Second, the high electronegativity of the nitrogen atoms in the isoalloxazine ring of riboflavin enhances electron affinity, promoting reversible reduction reactions.[27] These reactions induce coordination bonds between nitrogen atoms and cobalt ions, causing their adsorption onto the ZIF surface and suppressing crystal growth. The reduced particle size increases the limiting current density of the catalyst, thus enhancing ORR

activity.[32,33] In addition, a limited number of nanotubes were observed on the sample surface, originating from the high-temperature carbonization process. Zinc-ion migration promoted the movement of transition metal cobalt to the surface, which catalyzed the formation of nitrogen-doped carbon nanotubes (N-CNTs).[34–36] The nitrogen content in the Co_v–N–C_{850} reaches 20.83%, which is higher than that in the undoped C–N–C_{850}. This phenomenon is further substantiated by energy dispersive spectroscopy (EDS) analysis. Such a result implies that nitrogen atoms engage in condensation reactions with carbon rings during the pyrolysis process, thereby forming additional nitrogen-containing functional groups.

The transmission electron microscopy (TEM) images are shown in Fig. 2(d–h). The accurate lattice dimensions of the particles demonstrate that the lattice interval of the light gray area on the dodecahedron is 0.339 nm, corresponding to the C (002) crystal plane. This indicates the presence of a graphitized carbon structure, which is a typical feature of this material. The black regions distributed on the surface of the dodecahedron have a measured lattice spacing of 0.197 nm, which matches the crystal plane of metallic Co species (111). This finding suggests that during the pyrolysis process, Co^{2+} and Co^{3+} on the surface of the ZIF are converted into metallic Co species.[37,38] A porous, sponge-like structure has been observed
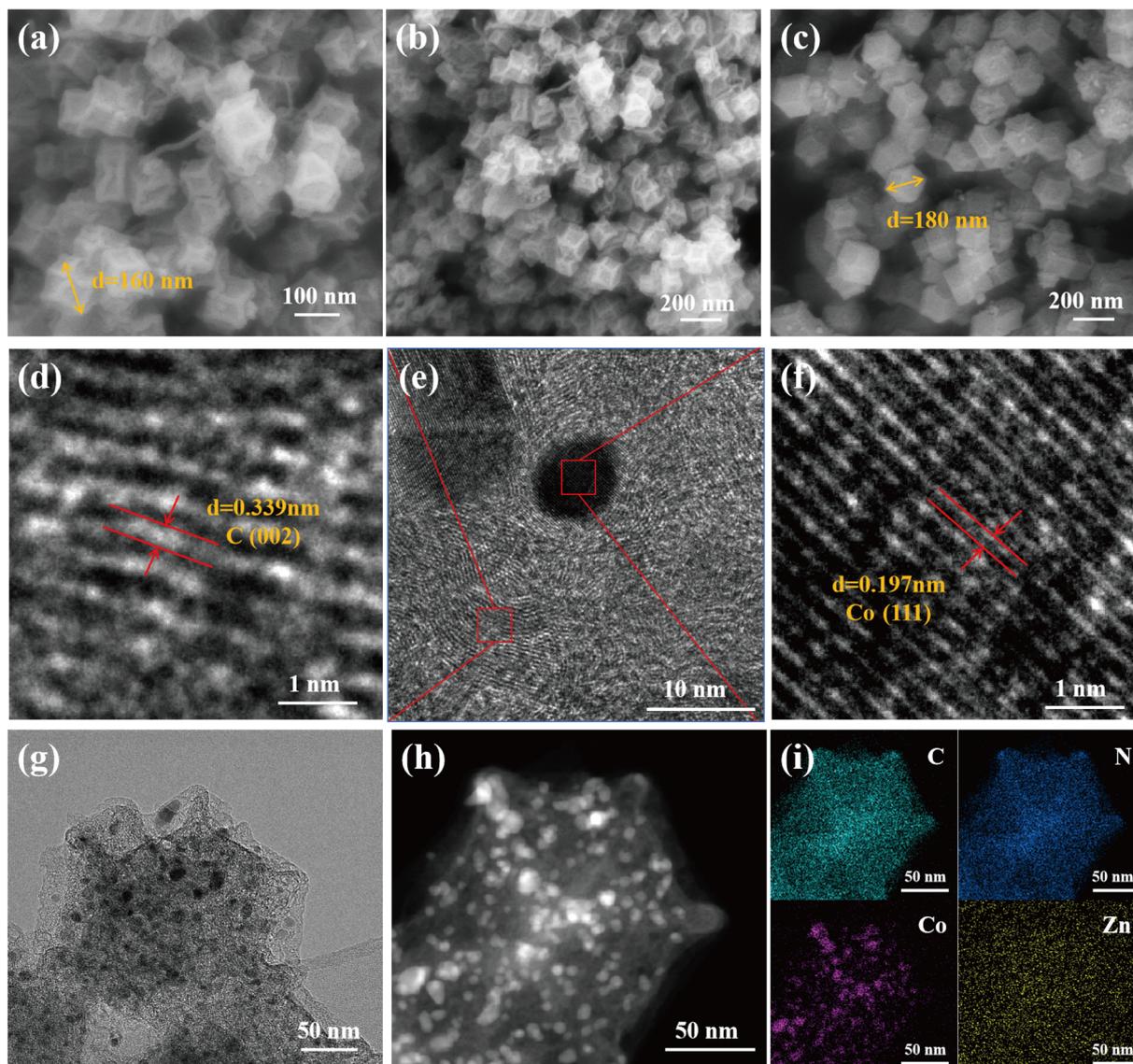
Fig. 2 (a and b) SEM images of Co_v-N-C_{850}, (c) SEM image of $Co-N-C_{850}$, (d–f) HRTEM images of $Co-N-C_{850}$, (g) TEM image of Co_v-N-C_{850}, (h) HAADF-STEM image of Co_v-N-C_{850}, and (i) the EDS mapping of the Co_v-N-C_{850} sample.

on the outer surface of the dodecahedron, formed by pyrolysis.[39,40] The amorphous nature of this structure is attributed to the residual carbon framework resulting from the thermal degradation of riboflavin.[41] Generally, the edge defects of this amorphous structure can provide active sites for oxygen reduction reactions while facilitating electron transport pathways, thereby enhancing the efficiency of mass transfer and charge transfer. The elemental composition of the catalyst, comprising carbon (C), nitrogen (N), oxygen (O), cobalt (Co), and zinc (Zn), was validated through high-angle annular dark field scanning transmission electron microscopy (HAADF-STEM) energy dispersive spectroscopy (Fig. 2i). Furthermore, the distribution of cobalt and nitrogen is uniform within the carbon framework, as revealed by the EDS mapping (Table S1†). In addition, some zinc is partially volati-

lized, resulting in its detection in the outer regions of the carbon structure. In summary, based on the SEM and TEM analysis, the active sites for the oxygen reduction reactions are uniformly embedded within the graphitized carbon framework, forming structural features with a dodecahedral morphology.

3.2 Physical properties and composition analysis

The thermal stability and structural changes of the Co_v-N-C_{850} catalyst during synthesis were determined through thermogravimetric analysis (TG) and differential thermogravimetric analysis (DTG) (Fig. S2†). Initially, the mass loss observed between 30 °C and 120 °C can be attributed to the evaporation of moisture. Subsequently, in the temperature range of 120 °C to 550 °C, the mass loss is primarily due to the removal of

three water molecules from the side chains, leading to the formation of a series of conjugated double bonds and the release of conjugated side chains.[42] As the temperature continues to rise, coordination occurs between the isoalloxazine ring and the metal ions within the ZIF structure. However, this configuration is unstable. Under high-temperature conditions, thermal degradation takes place, resulting in the cleavage of the isothiazole ring and C–N bonds. At approximately 850 °C, a significant number of carbon and nitrogen atoms are likely incorporated into the carbon matrix, yielding nitrogen-doped carbon residues.

As illustrated in Fig. 3a, Fourier transform infrared (FTIR) spectroscopy was utilized to examine the infrared absorption peaks of the Co_v–N–C, Co–N–C, ZIF-8&ZIF-67 precursors, and ZIF-8&ZIF-67-vb$_2$ precursors. The asymmetric telescopic vibrational signals of C–H, C=N in the imidazole ring, C=C in the imidazole ring, Co–N and Zn–N, were respectively identified in the peaks located at 3443.83 cm^{-1}, 1630.13 cm^{-1}, 1421.91 cm^{-1}, 1142.46 cm^{-1} and 756.16 cm^{-1} in the spectrum

of ZIF-8&ZIF-67.[43] Furthermore, the ZIF-8&ZIF-67-vb$_2$ spectrum exhibited C=O stretching vibrational absorption peaks at 1734.24 cm^{-1} and 1547.94 cm^{-1}.[25] This observation indicates that riboflavin has been effectively incorporated into the ZIF precursor structure. Following the application of heat treatment, the riboflavin and ZIF precursors underwent a process of carbonization, resulting in the complete absence of both the amide C=O and Zn–N telescoping peaks. Concomitantly, the C–H, C=N, C=C, and Co–N stretching vibrational peaks exhibited a certain degree of frequency shift. This alteration can be ascribed to the incorporation of nitrogen-containing functional groups into the carbon-backbone structure subsequent to the thermal decomposition of riboflavin.

As demonstrated by the X-ray diffraction (XRD) spectra (Fig. 3b), both Co_v–N–C and Co–N–C exhibit comparable diffraction peaks. This indicates that the introduction of riboflavin does not result in a significant alteration to the original crystalline structure of the catalyst. Moreover, the diffraction peak at 26° corresponds to the characteristic peak of the (002) plane
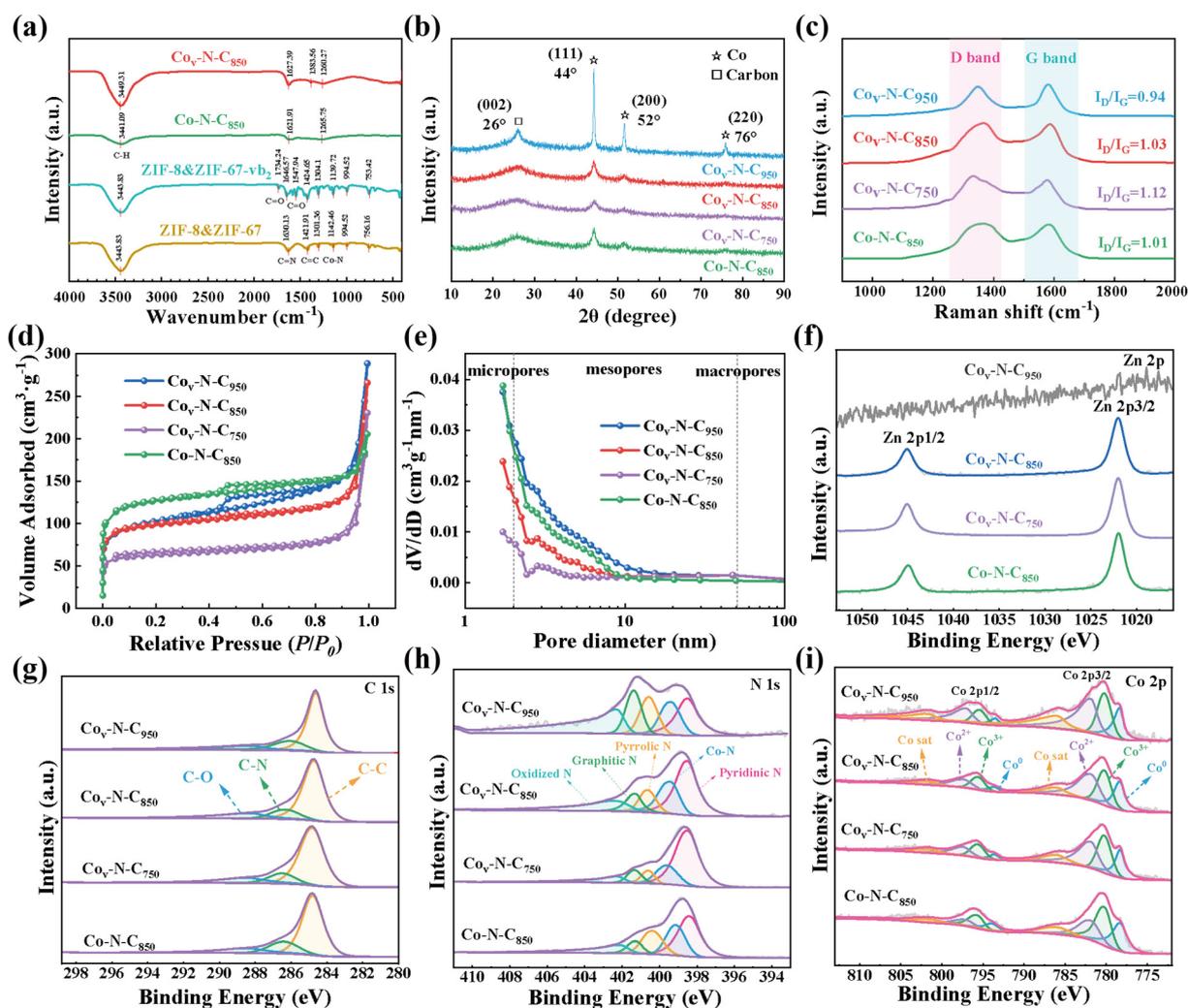

Fig. 3 (a) FTIR spectra, (b) XRD patterns, (c) Raman spectra, (d) N$_2$ sorption isotherms, and (e) pore size distributions based on the BJH method. XPS spectra (f) Zn 2p, (g) C 1s, (h) N 1s, (i) Co 2p for Co_v–N–C$_{750}$, Co_v–N–C$_{850}$, Co_v–N–C$_{950}$, and Co–N–C$_{850}$.

of graphitized carbon (PDF#41-1487), indicating a high degree of graphitization of the catalysts.[44] The diffraction peaks at 2θ angles of approximately 44°, 52°, and 76° are attributed to the (111), (200), and (220) crystal planes of metallic Co species (PDF#41-0943), respectively.[45,46] This confirms the presence of metallic Co species, which is consistent with the HRTEM results. Then, the results from Raman spectroscopy analysis of the four catalysts are presented in Fig. 3c. As the pyrolysis temperature is increased, the I_D/I_G ratio of Co_v–N–C is observed to decrease, indicating an enhancement in its degree of graphitization.[47] In comparison to Co–N–C_{850}, the I_D/I_G ratio of Co_v–N–C_{850} is slightly higher, which can be attributed to the introduction of nitrogen-containing functional groups into the carbon material following the decomposition of riboflavin, consequently increasing the defect density.

The porous structure of the catalyst material mainly consists of micropores and mesopores, as indicated by the nitrogen adsorption–desorption isotherms and pore size distribution diagrams (Fig. 3(d and e)).[48] As the pyrolysis temperature is increased, the micropore volume initially rises and then exhibits a slight decline, reaching a maximum of 0.13 cm^3 g^{-1} at 850 °C (Table S2†). In contrast, the mesopore volume continues to grow. This phenomenon can be attributed to the volatilization of zinc ions at their boiling point during the high-temperature pyrolysis process, leading to the formation of a microporous structure. In addition, the thermal degradation of riboflavin involves the cleavage of the isoalloxazine ring and C–N bonds, accompanied by the release of alcohols, ethylene, acetaldehyde, phenols, and CO$_2$. These processes, together with the defects induced by nitrogen doping, contribute significantly to the formation of mesopores.[49] These results are consistent with the TEM analysis. While Co_v–N–C_{850} exhibits a slightly smaller surface area compared to Co–N–C_{850}, it has a more complex mesoporous structure with a larger mesopore volume. The mesopore structure is conducive to medium transport, providing sufficient concentrations of reactants for the ORR. It is clear from the analysis of the XPS N 1s spectrum that the presence of more pyridinic N active sites in Co_v–N–C_{850} provides an abundance of adsorption sites for the reactant gases, significantly increasing the rate of the electrochemical reaction.

The elemental composition and binding energies of the four catalysts were analyzed by X-ray photoelectron spectroscopy (XPS) (Fig. S3†). The high-resolution Zn 2p spectrum, as illustrated in Fig. 3f, reveals the presence of two fitted peaks, situated at 1022.01 eV and 1045.05 eV, respectively.[50] As the pyrolysis temperature is increased, the concentration of zinc ions declines gradually. At a temperature of 850 °C, some Zn^{2+} ions coordinate with nitrogen atoms, forming a limited number of Zn–N$_x$ active sites, which contribute to an enhancement in the oxygen reduction activity of the samples. Concurrently, the volatilization of some zinc ions results in the formation of porous structures on the surface of the carbon material, thereby facilitating the mass transfer process of the samples.

The high-resolution C 1s spectrum is illustrated in Fig. 3g. The results of the spectral analysis indicate that the proportions of C–C bonds (284.80 eV), C–N bonds (286.40 eV), and C=O bonds (288.30 eV) in Co_v–N–C_{850} are 69.52%, 13.51%, and 16.98%, respectively.[51] The highest proportion of C–C bonds indicates that the carbon framework exhibits a high degree of graphitization and stability. Furthermore, the presence of C=O bonds provides additional confirmation of the successful incorporation of riboflavin.

The five fitting peaks in the high-resolution N 1s X-ray photoelectron spectrum (Fig. 3h) correspond to pyridinic nitrogen at 398.45 eV, cobalt–nitrogen bonds at 399.35 eV, pyrrolic nitrogen at 400.55 eV, graphitic nitrogen at 401.20 eV, and oxidized nitrogen at 402.20 eV, respectively.[52] The proportions of nitrogen-containing functional groups in the Co_v–N–C_{850} are 40.48%, 21.16%, 11.32%, 9.46%, and 17.58%, respectively. In comparison, the proportions in the Co–N–C_{850} are 37.78%, 22.24%, 18.39%, 7.42%, and 14.18%. It can be concluded that nitrogen exists primarily in the forms of pyridinic nitrogen and Co–N$_4$ molecules, both of which are considered to be active centers in the oxygen reduction reaction.[53] The intrinsic pyridinic and pyrrolic nitrogen structures present within the riboflavin molecular framework are integrated into the carbon skeleton during the doping of riboflavin and the subsequent thermal degradation process. This results in an increase in the content of pyridinic nitrogen, accompanied by the conversion of pyrrolic nitrogen to graphitic nitrogen, leading to an increase in the content of graphitic nitrogen. As a consequence, the oxygen reduction performance of the Co_v–N–C_{850} sample is enhanced.

The high-resolution map of Co 2p is presented in Fig. 3i. Notable peaks characteristic of metallic Co^0 are observed at 778.30 eV and 793.61 eV. A pair of Co^{2+} characteristic peaks are observed at 780.23 eV and 795.62 eV, while a pair of Co^{3+} characteristic peaks are observed at 781.84 eV and 797.29 eV. Furthermore, a pair of satellite peaks is identified at 785.90 eV and 801.69 eV.[54] The elevated concentration of Co^{2+} and Co^{3+} is conducive to the promotion of CoN$_x$ active site formation and the enhancement of the electrocatalytic activity of the samples in the oxygen reduction reaction.

3.3 Electrochemical performance

The ORR activity of Co–N–C was preliminarily assessed using cyclic voltammetry (CV). As demonstrated in Fig. S4,† the CV curves of all five catalysts in N$_2$-saturated KOH electrolyte did not exhibit any significant faradaic current response, indicating that no notable oxygen reduction reaction occurred under inert conditions. Conversely, in the same electrolyte saturated with O$_2$, all catalysts exhibited characteristic ORR peaks in the range of 0.7–0.8 V (vs. RHE), thereby confirming the efficient electrocatalytic performance for the oxygen reduction reaction. Further quantitative analysis of the characteristic peak potentials (Table S3†) revealed that the reduction peak potential of Co_v–N–C_{850} shifts positively to 0.746 V (vs. RHE), which is higher than that of the other catalysts. This preliminary finding suggests that Co_v–N–C_{850} possesses superior electrocatalytic activity for the oxygen reduction reaction compared to the other catalysts.

The rotating ring-disc electrode (RRDE) technique was employed to conduct linear sweep voltammetry (LSV) tests (Table S4†) in an alkaline electrolyte (0.1 M KOH) to analyze the ORR performance of various catalysts and Pt/C.[55,56] The impact of riboflavin doping on the catalytic oxygen reduction reaction performance is examined in Fig. 4b. The test results indicate that Co_v–N–C_{850} exhibits an onset potential of 0.929 V, a half-wave potential of 0.833 V, and a limiting current density of −5.132 mA cm^{-2}, outperforming the Co–N–C_{850} (E_{onset} = 0.919 V, $E_{1/2}$ = 0.812 V, j_L = −5.038 mA cm^{-2}) catalyst and showing comparable performance to Pt/C (E_{onset} = 0.935 V, $E_{1/2}$ = 0.825 V, j_L = −5.284 mA cm^{-2}) (Fig. 4c). The rise in nitrogen content in Co_v–N–C_{850} is accompanied by an increase in the number of active sites, which can be attributed to the influence of pyridinic and graphitic nitrogen concentrations on the ORR activity. This evidence suggests that riboflavin induces nitrogen doping. The limiting current density is influenced by the density of active sites and the hierarchical pore structure.[57,58] A comparison of Co–N–C_{850} and Co_v–N–C_{850}

reveals that the exposure of high-density Co–N$_4$ active sites in Co_v–N–C_{850} significantly enhances the kinetics of the ORR. At the same time, the optimized mesoporous structure improves the transport pathway for oxygen and accelerates the removal process of byproducts, facilitating the mass transfer process. In summary, the limiting current density is significantly increased, which in turn enhances the stability and activity of the catalyst at high current densities.

The performance of Co_v–N–C in ORR as a function of pyrolysis temperature is shown in Fig. 4a. The findings demonstrate that the optimal catalytic performance is achieved at a pyrolysis temperature of 850 °C. At this temperature, the Co–N$_4$ active sites play a significant role in the adsorption and dissociation of oxygen molecules, effectively reducing the activation energy of the ORR and enhancing its efficiency. At pyrolysis temperatures exceeding 850 °C, the primary conversion of pyridinic and pyrrolic nitrogen to graphitic nitrogen results in an increased degree of graphitization. However, this conversion is accompanied by a reduction in the number of active
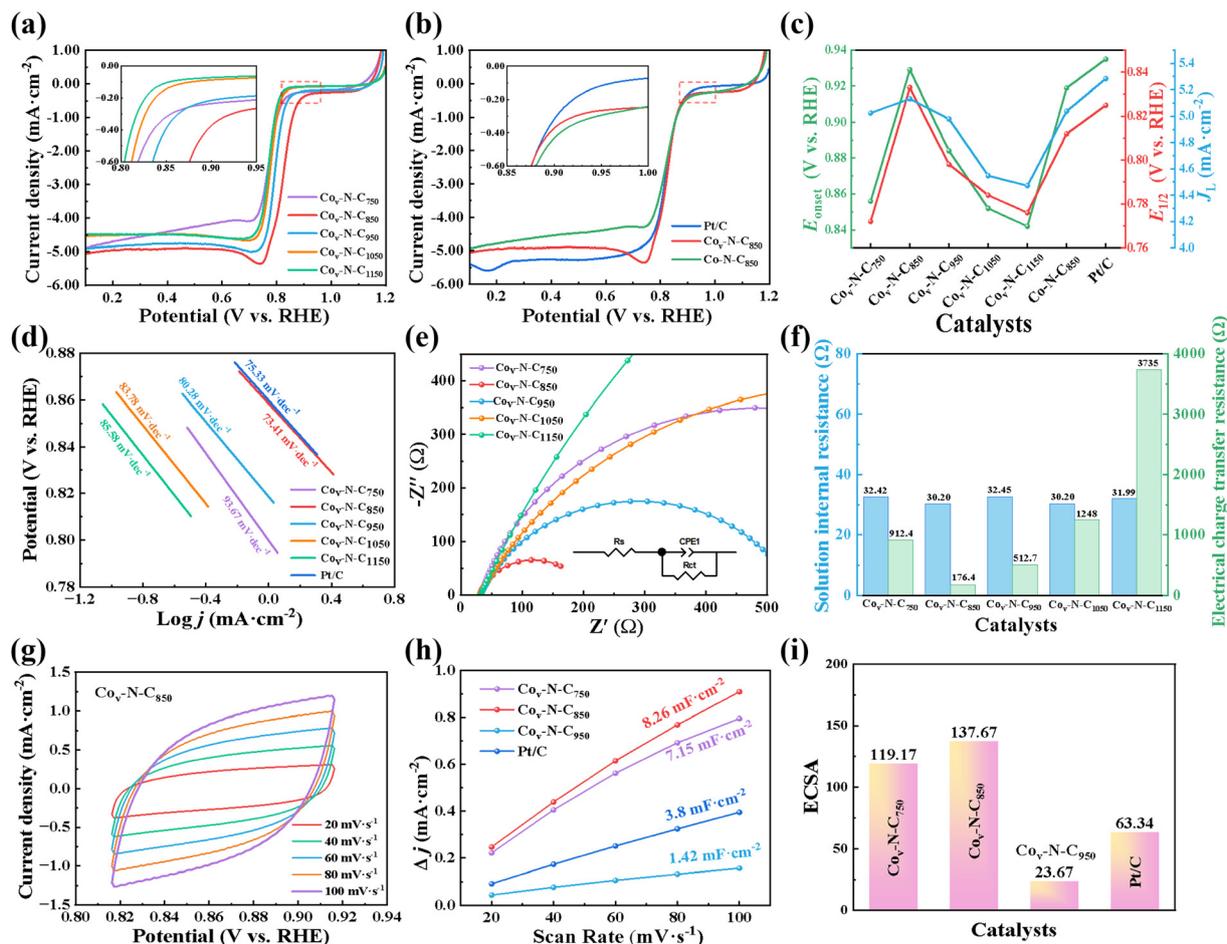

Fig. 4 (a and b) LSV curves in O$_2$-saturated 0.1 M KOH solution (scanning rate: 10 mV s^{-1}; rotation speed: 1600 rpm). (c) Onset potential, half-slope potential and limiting current density of various catalysts. (d) Tafel plots of the corresponding polarization curves, (e) EIS Nyquist plots for Co−N−C catalysts, and (f) solution internal resistance and charge transfer internal resistance of various catalysts. (g) Cyclic voltammetry curves of the Co_v−N−C_{850} in N$_2$-saturated 0.1 M KOH solution at different scan rates from 20 to 100 mV s^{-1}, (h) plots of current density against scan rates, and (i) the electrochemically active surface area (ECSA) for Co_v−N−C_{750}, Co_v−N−C_{850}, Co_v−N−C_{950}, and commercially available Pt/C, respectively.

sites, while the catalyst structure gradually collapses under high-temperature conditions, leading to a disruption of the dodecahedral structure and a decrease in mesoporous volume. This hinders the diffusion of oxygen and electrolytes. At a pyrolysis temperature of 750 °C, metallic zinc has not yet volatilized, and the mesoporous structure of the catalyst has not formed. This results in a lack of sufficient reactive space for the ORR and impedes effective mass transfer processes. This has a detrimental effect on the efficiency of the ORR and the activity of the catalyst.

Moreover, the electrochemical ORR performance in alkaline solutions was compared with that of other reported Co–N–C catalysts and non-metallic catalysts (Fig. S5 and Table S5†).[59–67] The results indicate that the Co_v–N–C_{850} electrode, prepared using the method outlined here, exhibits the optimal onset potential and half-wave potential, thereby demonstrating its superior ORR performance.

The Tafel slope fitting data presented in Fig. 4d demonstrates that the Tafel slope of Co_v–N–C_{850} is 73.41 mV dec^{-1}, which is comparable to that of Pt/C at 75.33 mV dec^{-1}. A reduced Tafel slope indicates that a higher current density can be achieved under conditions of lower overpotential.[68,69] The fitting analysis indicates that the Co_v–N–C_{850} catalyst displays comparable efficiency and kinetic performance to Pt/C. The electrochemical impedance spectroscopy (EIS) test curves are illustrated in Fig. 4e, which demonstrates the correlation between the radius of the semicircle and the charge transfer resistance. This correlation reflects the kinetic characteristics of the electrochemical reactions (Table S6†).[70,71] The observed data indicate that the solution resistance of the Co_v–N–C_{850} catalyst is 30.20 Ω, while the charge transfer resistance (R_{ct}) is 176.4 Ω (Fig. 4f). This is characterized by the smallest semicircular radius and is shown to have the lowest electron transfer impedance. This outcome corroborates the
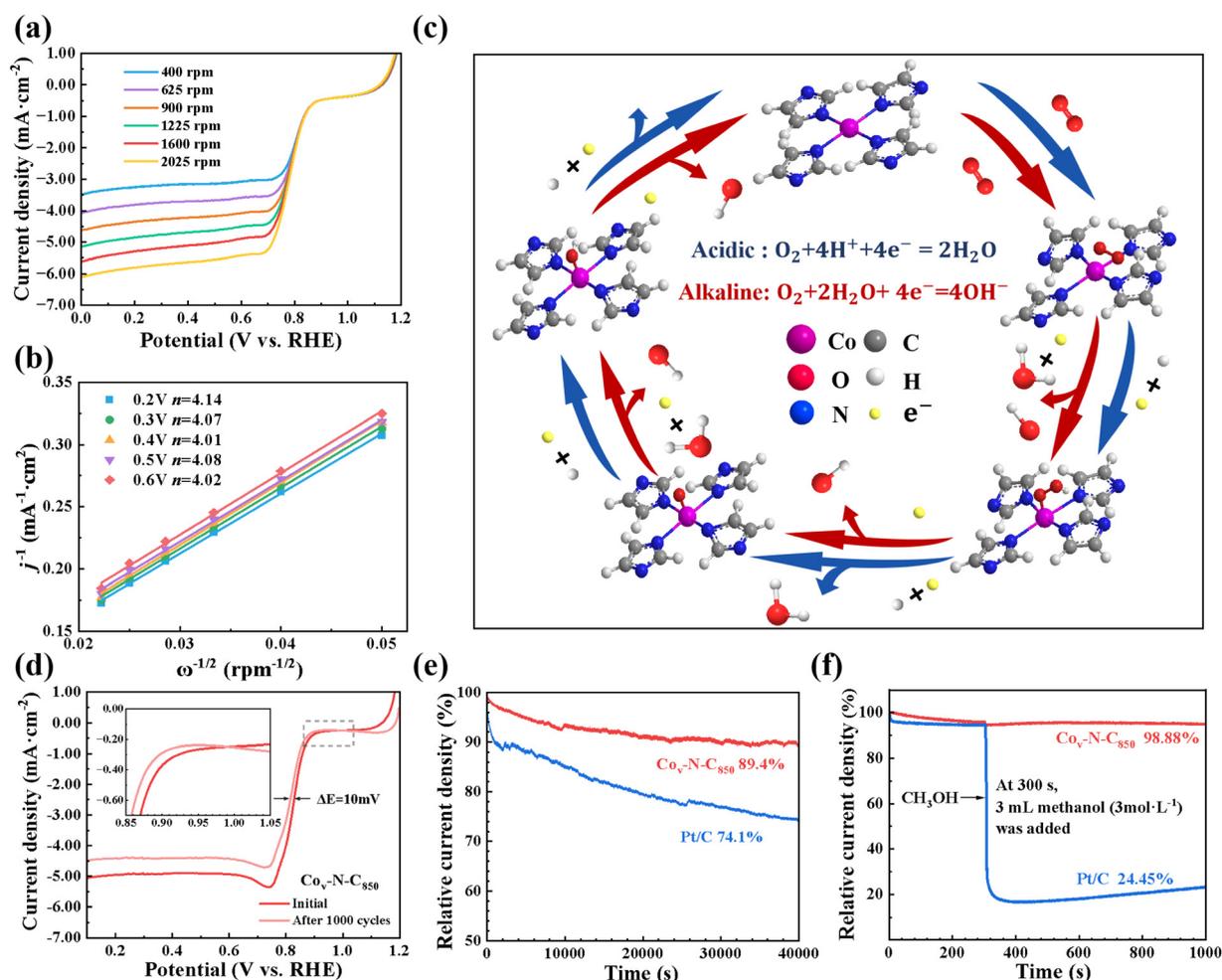

Fig. 5 (a) LSV curves of Co_v–N–C_{850} in 0.1 M O_2-saturated KOH electrolyte at different rotational speeds (from 400 to 2025 rpm) (scanning rate: 10 mV s^{-1}). (b) Koutecky–Levich profiles of Co_v–N–C_{850} obtained from (a) at 0.2–0.5 V. (The number of transferred electrons of Co_v–N–C_{850} at 0.2–0.5 V.) (c) The ORR mechanism of the Co–N–C catalyst. (d) Stability tests of Co_v–N–C_{850} before and after 1000 potential cycles. (e) Chronoamperometric measurement of Co_v–N–C_{850} and the commercially available Pt/C obtained at a fixed potential of 0.60 V in O_2-saturated 0.1 M KOH electrolyte at 1600 rpm. (f) Chronoamperometric responses of Co_v–N–C_{850} and commercially available Pt/C by injecting 2 wt% of methanol at 300 s.

findings of the linear sweep voltammetry measurements. To investigate the correlation between the electrochemical catalytic efficiency of Co_v–N–C_{850} and Pt/C and their electrochemically active surface area (ECSA), cyclic voltammetry curves were measured under specific potential ranges and different scan rates (Fig. 4(g–i)). Utilizing linear regression analysis, the double-layer capacitance (C_{dl}) and the ECSA were calculated under a saturated N_2 atmosphere with 0.1 M KOH electrolyte solution.[72,73] The ECSA value of Co_v–N–C_{850} was found to be 137.67, which is greater than that of Pt/C (23.67), indicating a greater abundance of electrochemically active sites. This outcome is closely associated with the elevated specific surface area and porous structural attributes exhibited by Co_v–N–C_{850}.

As demonstrated in Fig. 5(a and b), the limiting current density of all catalysts was found to be linearly fitted under varying rotation speeds, thereby revealing a linear increase in the limiting diffusion current density with increasing rotation speed.[74,75] The Koutecky–Levich (K–L) analysis was employed to determine the number of electron transfers. The K–L plots were used to calculate the electron transfer number (n) for the catalysts. The results show that Co_v–N–C_{850} has an electron transfer number of 4.06, while Co_v–N–C_{750} (n = 3.94), Co_v–N–C_{950} (n = 3.92), Co_v–N–C_{1050} (n = 3.63), and Co_v–N–C_{1150} (n = 3.47) all display electron transfer numbers below four (Fig. S6†). This indicates that Co_v–N–C_{850} demonstrates the best performance in terms of electron transfer number and kinetic activity, following a predominant four-electron transfer mechanism during the oxygen reduction reaction (Fig. 5c). An investigation was conducted into the ORR pathway for Co_v–N–C_{850}, utilizing a rotating ring-disk electrode (RRDE). As illustrated in Fig. S7,† the yield of H_2O_2 remained below 29.55% at all potentials, with an average electron transfer number of 3.41. This finding suggests that Co_v–N–C_{850} predominantly follows a four-electron transfer mechanism during the ORR process.

The results are presented in Fig. 5d, which illustrates that after 1000 cycles, the half-wave potential of Co_v–N–C_{850} exhibited a minimal negative shift of 10 mV.[76,77] Furthermore, the durability of Co_v–N–C_{850} was evaluated in comparison with Pt/C through the utilization of a chronoamperometric approach (i–t), as illustrated in Fig. 5e. Following a durability test of 40 000-seconds, the current density of Co_v–N–C_{850} was found to be 89.4% of its initial value, a performance that surpassed that of Pt/C, which exhibited a current density of 74.1%. The performance of the Co_v–N–C_{850} and Pt/C was evaluated through the measurement of the chronoamperometric response subsequent to the addition of methanol to the oxygen-saturated 0.1 M KOH solution at the 300 second interval.[78] As illustrated in Fig. 5f, following a testing period of 1000 seconds, the Co_v–N–C_{850} exhibited a current density of 98.88% of its initial value, whereas the Pt/C catalyst demonstrated a notable decline, reaching only 24.45% of its initial current density. This result indicates that the Co_v–N–C_{850} possesses excellent resistance to methanol permeation.

4 Conclusion

In this study, riboflavin was employed as a nitrogen precursor to synthesize a porous carbon electrode containing efficient and uniformly dispersed Co–N_4 active sites. During high-temperature pyrolysis, nitrogen derived from riboflavin promoted progressive condensation and self-assembly of the carbon framework, enhancing the formation of catalytically active nitrogen-containing functional groups. The resulting material exhibited significantly improved electrocatalytic ORR performance. The study demonstrates that optimizing riboflavin doping yields a Co–N–C catalyst with a highly graphitized carbon structure, a large electrochemically active surface area, efficient oxygen/electron transport kinetics, a dominant four-electron-transfer pathway, remarkable durability and methanol tolerance, alongside exceptional ORR catalytic activity.

Data availability

The data that support the findings of this study are available from the corresponding authors upon reasonable request.

Conflicts of interest

There are noconflicts to declare.

Acknowledgements

References

1 Q. Gou, H. Luo, L. Qu, F. Yu, K. Wang, S. Zhang, Z. Luogu, B. Zhang, Y. Zheng and B. Song, *J. Energy Chem.*, 2025, **101**, 191–200.

2 S. Zhang, Q. Gou, W. Chen, H. Luo, R. Yuan, K. Wang, K. Hu, Z. Wang, C. Wang and R. Liu, *Adv. Sci.*, 2024, **11**, 2404968.

3 Q. Gou, Z. Chen, H. Luo, J. Deng, B. Zhang, N. Xu, J. Cui, Y. Zheng, M. Li and J. Li, *Small*, 2024, **20**, 2305902.

4 C. Li, Q. Gou, R. Tang, J. Deng, K. Wang, H. Luo, J. Cui, Y. Geng, J. Xiao and Y. Zheng, *J. Phys. Chem. Lett.*, 2023, **14**, 9150–9158.

5 J. Lian, J.-Y. Zhao and X.-M. Wang, *Acta Metall. Sin.*, 2021, **34**, 885–899.

6 M. Arif, A. Mahsud, T. Muhmood and F. L. Deepak, *J. Environ. Chem. Eng.*, 2024, 113417.

7 J. Xiong, X. Chen, Y. Zhang, Y. Lu, X. Liu, Y. Zheng, Y. Zhang and J. Lin, *RSC Adv.*, 2022, **12**, 2425–2435.

8 C. Yang, X. Ma, J. Zhou, Y. Zhao, X. Xiang, H. Shang and B. Zhang, *Int. J. Hydrogen Energy*, 2022, **47**, 21634–21661.

9 J. Wang, Y. Wang, H. Hu, Q. Yang and J. Cai, *Nanoscale*, 2020, **12**, 4238–4268.

10 M. A. Mohamud and A. B. Yurtcan, *Int. J. Hydrogen Energy*, 2021, **46**, 33782–33800.

11 R. Haider, S. Ding, W. Wei, Y. Wan, Y. Huang, R. Li, L. Wu, A. Muzammil, Y. Fan and X. Yuan, *J. Mater. Chem. A*, 2023, **11**, 18387–18397.

12 D. Xili, Q. Zhou and L. Zhang, *J. Alloys Compd.*, 2022, **911**, 165072.

13 B.-Y. Song, M.-J. Li, Y.-W. Yang and Y.-L. He, *J. Cleaner Prod.*, 2020, **249**, 119314.

14 H. Luo, Q. Gou, Y. Zheng, K. Wang, R. Yuan, S. Zhang, W. Fang, Z. Luogu, Y. Hu and H. Mei, *ACS Nano*, 2025, **19**, 2427–2443.

15 Q. Guo, S. Zhang, H. Mei, C. Liu, H. Luo, K. Wang, Y. Hu, B. Song, Y. Zheng and M. Qiao, *J. Mater. Chem. A*, 2025, **13**, 7766–7776.

16 P. Wei, X. Li, Z. He, X. Sun, Q. Liang, Z. Wang, C. Fang, Q. Li, H. Yang and J. Han, *Chem. Eng. J.*, 2021, **422**, 130134.

17 Z. M. Siahkalroudi, B. Aghabarari, M. Vaezi, E. Rodríguez-Castellón and M. V. Martínez-Huerta, *Mol. Catal.*, 2021, **502**, 111372.

18 D. Yuan, Y. Li, Q. She and X. Zhu, *Colloids Surf., A*, 2023, **663**, 131105.

19 L. Ye, Y. Ying, D. Sun, J. Qiao and H. Huang, *Nanoscale*, 2022, **14**, 2065–2073.

20 J. Wang, J. Guoa, Y. Y. Liua, P. Lia, Q. Fanga, X. C. Li and W. Song, *ChemPhysChem*, 2024, **25**, e202400414.

21 Z. Wu, M. Song, J. Wang and X. Liu, *Catalysts*, 2018, **8**, 196.

22 X. Ren, B. Liu, X. Liang, Y. Wang, Q. Lv and A. Liu, *J. Electrochem. Soc.*, 2021, **168**, 044521.

23 D. W. Kim, S. Heo, J. S. Lee and S. Y. Lim, *Electrochem. Commun.*, 2021, **129**, 107092.

24 J. Shi, R. Wu, Y. Li, J. Wu, Y. Kuang, H. Xing, Y. Zhang and K. Hui, *Diamond Relat. Mater.*, 2024, **141**, 110700.

25 Y. Deng, H. Huangfu, S. Tang and J. Li, *Chin. J. Catal.*, 2017, **38**, 1668–1679.

26 P. Sekar, P. Vasanthakumar, R. Shanmugam, S. S. Kumar, S. Agnoli, R. J. Deepak, K. Murugan, N. Bhuvanesh and R. Karvembu, *Green Chem.*, 2022, **24**, 9233–9244.

27 L. Cheng, Y. Liang, Q. Zhu, D. Yu, M. Chen, J. Liang and H. Wang, *Chem. – Asian J.*, 2020, **15**, 1290–1295.

28 K. Lin, R. Gómez-Bombarelli, E. S. Beh, L. Tong, Q. Chen, A. Valle, A. Aspuru-Guzik, M. J. Aziz and R. G. Gordon, *Nat. Energy*, 2016, **1**, 1–8.

29 N. Ahmad, M. Alam and M. A. N. Al-Otaibi, *Prog. React. Kinet. Mech.*, 2015, **40**, 86–94.

30 J. Masłowska and M. Malicka, *J. Therm. Anal.*, 1987, **32**, 1659–1665.

31 D. Kim, J. Park, J. Park, J. Jang, M. Han, S. H. Lim, D. Y. Ryu, J. You, W. Zhu and Y. Yamauchi, *Small Methods*, 2024, 2400236.

32 J. Martínez-Loyola, M. Carrasco-Cordero, I. Alonso-Lemus, F. Rodríguez-Varela, P. Bartolo-Pérez, B. Escobar-Morales, Y. Vega-Cantú and F. Rodríguez-Macías, *Electrochem. Commun.*, 2024, **166**, 107792.

33 C. Yong, Y. Xu, H. Yu, P. Wu, J. Wang, L.-L. Shen, G.-R. Zhang and D. Mei, *J. Catal.*, 2023, **428**, 115148.

34 Y. Zhang, T. Zhu, Q. Zhong and H. Qu, *J. Alloys Compd.*, 2023, **958**, 170447.

35 Y. Zhang, M. Yang, P. Wang, K. Li, S. Li, Z. Zhang, X. He and Y. Duan, *J. Alloys Compd.*, 2022, **904**, 164083.

36 G. Li, W. Deng, L. He, J. Wu, J. Liu, T. Wu, Y. Wang and X. Wang, *ACS Appl. Mater. Interfaces*, 2021, **13**, 28324–28333.

37 Z.-G. Yang, H.-M. Xu, T.-Y. Shuai, Q.-N. Zhan, Z.-J. Zhang, K. Huang, C. Dai and G.-R. Li, *Nanoscale*, 2023, **15**, 11777–11800.

38 K. Li, Y. Zhang, P. Wang, X. Long, L. Zheng, G. Liu, X. He and J. Qiu, *J. Alloys Compd.*, 2022, **903**, 163701.

39 S. S. Sekhon, J. Lee and J.-S. Park, *J. Energy Chem.*, 2022, **65**, 149–172.

40 Y. Zhao, X. Liu, Y. Liu, Y. Chen and S. Gao, *Int. J. Hydrogen Energy*, 2022, **47**, 12964–12974.

41 X. Hu, L.-L. Ma, W.-J. Liu, H.-C. Li, M.-M. Ma and H.-Q. Yu, *Sci. Total Environ.*, 2021, **782**, 146844.

42 J. Masłowska and M. Malicka, *J. Therm. Anal.*, 1988, **34**, 3–9.

43 A. Bharti and R. Natarajan, *ChemistrySelect*, 2021, **6**, 2298–2305.

44 X. Hu, X. Chen, X. Li and C. Xu, *Adv. Funct. Mater.*, 2024, 2316699.

45 T. Zhang, F. Cheng, C. Zhao, H. Liu, X. Song, X. Li and W. Luo, *ACS Appl. Mater. Interfaces*, 2021, **13**, 52167–52173.

46 Z. Wu, X. Hu, C. Cai, Y. Wang, X. Li, J. Wen, B. Li and H. Gong, *J. Colloid Interface Sci.*, 2024, **657**, 75–82.

47 S. Kumar, R. Kumar, N. Goyal, A. Vazhayil, A. Yadav, N. Thomas and B. Sahoo, *ACS Appl. Nano Mater.*, 2024, **7**, 7865–7882.

48 M.-Y. Yu, Y.-F. Yao, K. Fang, L.-S. Chen, L.-P. Si and H.-Y. Liu, *ACS Appl. Mater. Interfaces*, 2024, **16**, 16132–16144.

49 X. Hu, R. Wang, W. Feng, C. Xu and Z. Wei, *J. Energy Chem.*, 2023, **81**, 167–191.

50 G. Singla, S. N. Bhange, M. Mahajan and S. Kurungot, *Nanoscale*, 2021, **13**, 6248–6258.

51 L. Yang, J. Ma, Y. Liu, C. Ma, X. Yu and Z. Chen, *Nanoscale*, 2024, **16**, 5433–5440.

52 Y. Yang, J. Lou, Y. Zhao, J. Wei, Y. Zhou, C. Zhang, M. Wu, Y. Zhang, Q. Wang and L. Wang, *Chem. Eng. J.*, 2023, **477**, 146900.

53 Z. Li, H. Yu, Y. Zhang, D. Wu, Y. Bai, S. Liu and H. Zhao, *Chem. Commun.*, 2023, **59**, 4535–4538.

54 X. Liu, W. Yan, J. Song, H. Song, W. Chen, Y. Zhang and Y. Chen, *Chem. Eng. J.*, 2024, **492**, 152301.

55 J. Xue, Z. Liu and Y. Li, *J. Energy Storage*, 2023, **74**, 109343.

56 X. Hu, W. Tian, Z. Wu, X. Li, Y. Li and H. Wang, *J. Colloid Interface Sci.*, 2024, **672**, 610–617.

57 Q. Wang, C. Wang, K. Zheng, B. Wang, Z. Wang, C. Zhang and X. Long, *Angew. Chem., Int. Ed.*, 2024, **63**, e202320037.

58 Z. You, B. Wang, Z. Zhao, Q. Zhang, W. Song, C. Zhang, X. Long and Y. Xia, *Adv. Mater.*, 2023, **35**, 2209129.

59 P.-Y. Jiang, Z.-H. Xiao, Y.-F. Wang, N. Li and Z.-Q. Liu, *Bioelectrochemistry*, 2021, **138**, 107717.

60 L. Zhang, J. Yuan, Q. Xu, F. Zhang, Q. Sun and H. Xie, *Int. J. Biol. Macromol.*, 2023, **242**, 125110.

61 Y. Ruan, H. Xu, H. Lei, W. Xue, T. Wang, S. Song, Y. Yu, G.-R. Zhang and D. Mei, *Inorg. Chem. Front.*, 2023, **10**, 2370–2379.

62 L. Li, G. Han, Y. Wen, Y. Liu, R. Xiao, W. Zhang, F. Kong, L. Du, Y. Ma and P. Zuo, *Fuel*, 2023, **345**, 128199.

63 Q.-R. Pan, P.-Y. Jiang, B.-L. Lai, Y.-B. Qian, L.-J. Huang, X.-X. Liu, N. Li and Z.-Q. Liu, *Chemosphere*, 2022, **291**, 132701.

64 F. Li, X.-B. Ding, Q.-C. Cao, Y.-H. Qin, L. Yang and C.-W. Wang, *Int. J. Hydrogen Energy*, 2022, **47**, 3762–3770.

65 D. Li, B. Wang, X. Long, W. Xu, Y. Xia, D. Yang and X. Yao, *Angew. Chem.*, 2021, **133**, 26687–26692.

66 J. Yang, F. Xiang, H. Guo, L. Wang and X. Niu, *Carbon*, 2020, **156**, 514–522.

67 G. Chao, Y. Zhang, L. Zhang, W. Zong, N. Zhang, T. Xue, W. Fan, T. Liu and Y. Xie, *J. Mater. Chem. A*, 2022, **10**, 5930–5936.

68 J. Xue, Z. Liu, Y. Fan, R. Wang and Y. Li, *Chem. Eng. J.*, 2023, **476**, 146502.

69 J. Deng, H. Luo, Q. Gou, J. Wang, Z. Chen, N. Xu, Z. Liu, Y. He, Z. Luogu and G. Jiang, *J. Phys. Chem. Lett.*, 2023, **14**, 9167–9175.

70 F. Li, J. Niu, Y. Liu, T. Qin, D. Zhao, Q. Zhao and X. Liu, *J. Power Sources*, 2023, **553**, 232310.

71 B. Liang, M. Su, Z. Zhao and S.-X. Liang, *J. Electroanal. Chem.*, 2024, **962**, 118260.

72 X. He, L. Chang, H. Wu, G. Liu, Y. Zhang and A. Zhou, *J. Alloys Compd.*, 2023, **967**, 171709.

73 X. Zhao, X. Maimaitiyiming, A. Sawut and Z. Kuerban, *Int. J. Hydrogen Energy*, 2024, **77**, 1268–1275.

74 X. Yao, X. Wang, L. Sun, L. Li, E. Kan, B. Ouyang and W. Zhang, *Inorg. Chem. Front.*, 2022, **9**, 2517–2529.

75 Y. Liu, Y. Zheng, P. Zhang and J. Hou, *Molecules*, 2023, **29**, 3.

76 Y. Zhou, Y. Yu, D. Ma, A. C. Foucher, L. Xiong, J. Zhang, E. A. Stach, Q. Yue and Y. Kang, *ACS Catal.*, 2020, **11**, 74–81.

77 X. Zhang, C. Gao, L. Li, X. Yan, N. Zhang and J. Bao, *J. Colloid Interface Sci.*, 2024, **676**, 871–883.

78 H. Lv, P. Tong, H. Li, B. Sun, Y. Li, P. Qiao, H. Tian and H. Xia, *Chem. Eng. J.*, 2023, **478**, 147375.